Eur. Phys. J. A **41**, 315–321 (2009)
DOI 10.1140/epja/i2009-10817-3

THE EUROPEAN PHYSICAL JOURNAL A

Regular Article – Experimental Physics

Charge radii and magnetic moments of odd-A $^{183-189}$Pb isotopes

M.D. Seliverstov[1,2,a], A.N. Andreyev[3,4,5], N. Barré[6], A.E. Barzakh[2], S. Dean[5], H. De Witte[5], D.V. Fedorov[2], V.N. Fedoseyev[7], L.M. Fraile[7,b], S. Franchoo[1,6], J. Genevey[8], G. Huber[1], M. Huyse[5], U. Köster[7,9], P. Kunz[1], S.R. Lesher[5,c], B.A. Marsh[7,10], I. Mukha[5,d], B. Roussière[6], J. Sauvage[6], I. Stefanescu[5,e], K. Van de Vel[5,f], P. Van Duppen[5], and Yu.M. Volkov[2]

[1] Institut für Physik, Johannes Gutenberg Universität, D-55099 Mainz, Germany
[2] Petersburg Nuclear Physics Institute, 188350 Gatchina, Russia
[3] Oliver Lodge Laboratory, University of Liverpool, Liverpool, L69 7ZE, UK
[4] TRIUMF, Vancouver BC, V6T 2A3, Canada
[5] Instituut voor Kern- en Stralingsfysica, K.U. Leuven, B-3001 Leuven, Belgium
[6] Institut de Physique Nucléaire, IN2P3-CNRS/Université Paris-Sud, F-91406 Orsay Cedex, France
[7] ISOLDE,CERN, CH-1211 Genève 23, Switzerland
[8] Laboratoire de Physique subatomique et de cosmologie, IN2P3-CNRS/Université Joseph Fourier, F-38026 Grenoble Cedex, France
[9] Institut Laue-Langevin, F-38042 Grenoble Cedex 9, France
[10] Department of Physics, University of Manchester, Manchester, M60 1QD, UK

Received: 16 April 2009
Published online: 12 July 2009 –
Communicated by B.R. Fulton

Abstract. Isotope shifts and hyperfine splitting parameters have been measured for the neutron-deficient odd-mass lead isotopes $^{183-189}$Pb. The measurement was performed at the ISOLDE (CERN) online mass separator using the in-source resonance ionization spectroscopy technique. The nuclear root mean square charge radii $\langle r^2 \rangle$ and the electromagnetic moments μ and Q_S have been deduced. They follow the smooth trend of the heavier isotopes and indicate the absence of deformation.

PACS. 21.10.Ky Electromagnetic moments – 27.70.+q $150 \leq A \leq 189$ – 32.10.Fn Fine and hyperfine structure – 42.62.Fi Laser spectroscopy

1 Introduction

The structure of the neutron-deficient Pb isotopes with closed proton shell ($Z = 82$) exhibits single-particle as well as collective behaviour at low excitation energy. Shape coexistence, caused by proton pair excitations across the $Z = 82$ shell gap, has been observed around $N = 104$ as exemplified by ^{186}Pb, where triple shape coexistence was reported [1]. Extensive decay and in-beam studies (*e.g.* [2–4] and references therein) of the excited states in the lead isotopes confirmed the coexistence of different spherical and deformed structures at low excitation energy.

Laser spectroscopy is a powerful method which directly sheds light on this phenomenon. Isotope shift measurements provide information on the variation of the nuclear rms charge radius along an isotopic series. Measurements of hyperfine splitting of atomic lines give the nuclear magnetic and spectroscopic quadrupole moments that provide information on the nuclear structure and deformation, respectively [5,6].

Prior to our studies charge radii and electromagnetic moments have been measured for Pb isotopes with $A \geq 190$ only [7,8]. In our previous paper [9] the charge radii for the even-A $^{182-190}$Pb isotopes were discussed. We concluded from a comparison of the data with calculations that the lead isotopes are essentially spherical in their ground states.

It is well known that studies of odd-A nuclei provide valuable information on shape coexistence, as was demonstrated by the pronounced shape staggering for $^{185-187}$Hg, first observed by means of optical spectroscopy [10]. It is therefore of great interest to investigate the neighbouring

[a] e-mail: maxim.seliverstov@cern.ch
[b] *Present address:* Universidad Complutense, Madrid, Spain.
[c] *Present address:* Lawrence Livermore National Laboratory, Livermore, CA 94551, USA.
[d] *Present address:* Universidad de Sevilla, Sevilla, Spain.
[e] *Present address:* ANL, Argonne, IL 60439, USA.
[f] *Present address:* VITO, IMS, Mol, Belgium.

odd-A Pb isotopes. The present work reports the experimental data and the analysis procedures used for the odd-A $^{183-189}$Pb isotopes. The data were obtained during the same experiment as presented in ref. [9].

The in-source photo-ionization spectroscopy technique is a very sensitive laser spectroscopy method and can therefore be used to study isotopes with extremely low production yields [11–13]. This technique, in combination with efficient isotope and isomer selective registration of the photo-ions by means of nuclear spectroscopy, is essential for the light Pb isotopes region where prominent isomerism is established. Based on in-beam and decay studies, and the level systematics of heavier odd-A isotopes, the occurrence of low-spin ($I^\pi = 3/2^-$) ground state and high-spin ($I^\pi = 13/2^+$) isomeric states is expected in $^{183-189}$Pb. However, no direct measurements (with the exception of ^{185}Pb [14]) have previously been performed.

2 Experiment

The Pb nuclei were produced in spallation reaction induced by a 1.4 GeV proton beam impinging on a UC_x target (50 g/cm^2 of ^{238}U) connected to the Resonance Ionization Laser Ion Source, RILIS, of the ISOLDE mass separator. The spallation products diffused out of the high-temperature target ($T \approx 2050\,^\circ$C) and effused as neutral atoms into the laser ion source cavity. The cavity, a niobium tube of 30 mm length and 3 mm internal diameter, was heated to approximately 2100 °C. The laser beams were focused inside the cavity and Pb isotopes were ionized with a three-step photo-ionization scheme (see fig. 1). An ionization efficiency of 3% has been measured offline [15] for this scheme. After photo-ionization, acceleration to 60 keV and mass separation, the ions were implanted in one of the detection systems available.

Laser light for the resonant excitation of the first two atomic transitions was provided by two tunable pulsed dye lasers. The ultraviolet radiation was obtained by doubling the frequency of the fundamental dye laser radiation using a non-linear BBO crystal. Copper vapour lasers operating at a pulse repetition rate of 11 kHz were used to pump the dye lasers and to perform the excitation from the second excited state into the continuum (the third step). The laser power for the first excitation step was reduced to avoid line broadening caused by saturation. This results in a reduction of the photo-ion current by a factor of 2.5–3.

For the atomic spectroscopy measurements, a narrow bandwidth laser (with linewidth before frequency doubling of 1.2 GHz) was used for the first excitation step, the linewidth of the second step laser was more than 20 GHz. Whilst counting the mass-separated photo-ions, the frequency ν_L of the first-step laser was scanned. In this way the isotope shifts and hyperfine splitting of the $6p^2\ ^3P_0 \rightarrow 6p7s\ ^3P_1^o$ ($\lambda_1 = 283.305$ nm) atomic spectral line were measured.

Two counting set-ups located at two different beam lines of the ISOLDE mass separator were used. The first one consisted of a "wind-mill" system in which the radioactive beam was implanted in thin (20 μg/cm^2) carbon

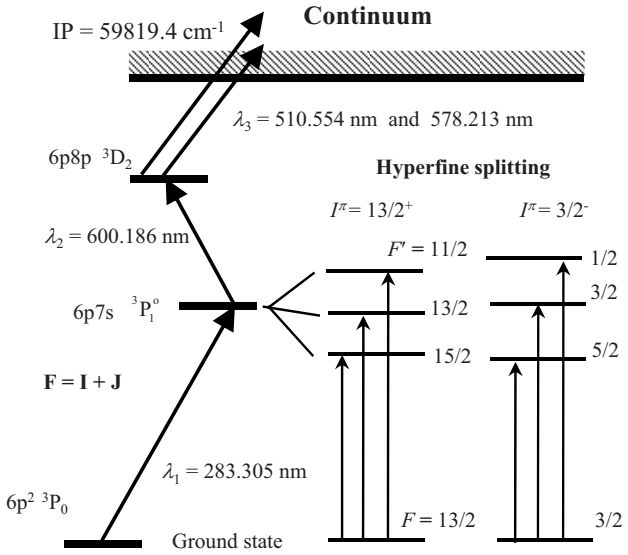

Fig. 1. The three-step laser ionization scheme for Pb isotopes applied in this work. The electronic configurations for the levels involved and the laser wavelengths for each step are shown. On the right a schematic illustration of the hyperfine structure in the case of the $13/2^+$ and $3/2^-$ states in odd-A Pb nuclei is presented. The three hfs lines expected for $I = 13/2$ and $I = 3/2$ are also shown.

foils mounted on a rotating wheel. A Si detector was placed behind the foil to measure the α-radiation during a fixed implantation time ($t_{measr} = t_{impl}$). This set-up was used for measurements on the α-decaying $^{182-188}$Pb isotopes. Details are described in ref. [9]. In the second set-up, the radioactive ions were implanted in a tape station and transported to a set of α, β and γ detectors. This set-up was used for $\beta\gamma\gamma$ measurements of the longer-lived ^{189,190}Pb ($T_{1/2} > 50$ s). More experimental details and a discussion of the obtained nuclear spectroscopy data for the ^{189}Pb decay are given in a separate paper [16].

The number of photo-ions produced was obtained by counting either α-particles (wind-mill station) or α-particles and/or γ-rays emitted (tape station). For every laser frequency setting an α- or γ-ray spectrum was recorded and the characteristic decay lines (E_α, E_γ; see table 1) were integrated. In this way the optical photo-ionization spectra (number of photo-ions *vs.* laser frequency) were obtained (see fig. 2).

For the measurements of low-intensity radioactive ion beams it is essential to ensure stable and reproducible laser frequency control and stabilization. For this purpose a multiparameter servo-control for the laser frequency scanning was implemented. This system incorporates controls for the narrow-band laser etalon and diffraction grating positions, a frequency read-out (wavemeter ATOS LM007) with feed-back control and communication to the α-, β- and γ-spectroscopy data acquisition system. The long-term stability of the laser control system enabled laser scans in excess of two hours to be performed. More details on the laser set-up are given in refs. [13,17,18].

Table 1. Properties of the lead isotopes [14,19–29] used for the atomic spectroscopy measurements and the parameters of the experimental set-up.

Isotope	I^π	$T_{1/2}$ (s)	b_α (%)	E_α (E_γ for $A \geq 189$)[a] (keV)	Implantation (measurement) time[b] t_{impl}, (t_{measr}) (s)	Yield (ions/μC)
^{182}Pb	0^+	0.055(5)	≤ 100	6911(10)	180	10^{-1}
^{183}Pb	$3/2^-$	0.535(30)	100	6570(10), 6775(7)	168	10
^{183m}Pb	$13/2^+$	0.415(20)	100	6698(5)	168	40
^{184}Pb	0^+	0.480(25)	80(15)	6626(6)	16.8	5×10^2
^{185}Pb	$3/2^-$	6.3(4)	50(25)	6288(5)	16.8	4×10^2
^{185m}Pb	$13/2^+$	4.3(2)	50(25)	6408(5)	16.8	1.5×10^3
^{186}Pb	0^+	4.79(5)	38(9)	6335(10)	33.6	10^4
^{187}Pb	$3/2^-$	15.2(3)	9.5(20)	6194(10), 6258(19)	16.8	4×10^4
^{187m}Pb	$13/2^+$	18.3(3)	12(2)	6073(10)	16.8	5×10^4
^{188}Pb	0^+	25.1(1)	8.0(6)	5980(10)	16.8	2×10^5
^{189}Pb	$3/2^-$	50(3)[c]	~ 0.4	667.4	2.5 (54)	–[d]
^{189m}Pb	$13/2^+$	39(8)[c]		386.2, 480.3, 700.4	2.5 (54)	–[d]
^{190}Pb	0^+	72(6)	0.40(4)	942	10 (240)[e]	–[d]

[a] Only lines used in the analysis are shown.
[b] Measurement time (t_{measr}) is shown in brackets, if the implantation (t_{impl}) and measurement times are different.
[c] Data for the ^{189}Pb decay obtained in our study are given in a separate paper [16].
[d] No absolute calibration of the detector efficiency has been performed.
[e] Five implantations ($t_{impl} = 2$ s) with total $t_{measr} = 240$ s were made for each laser frequency setting.

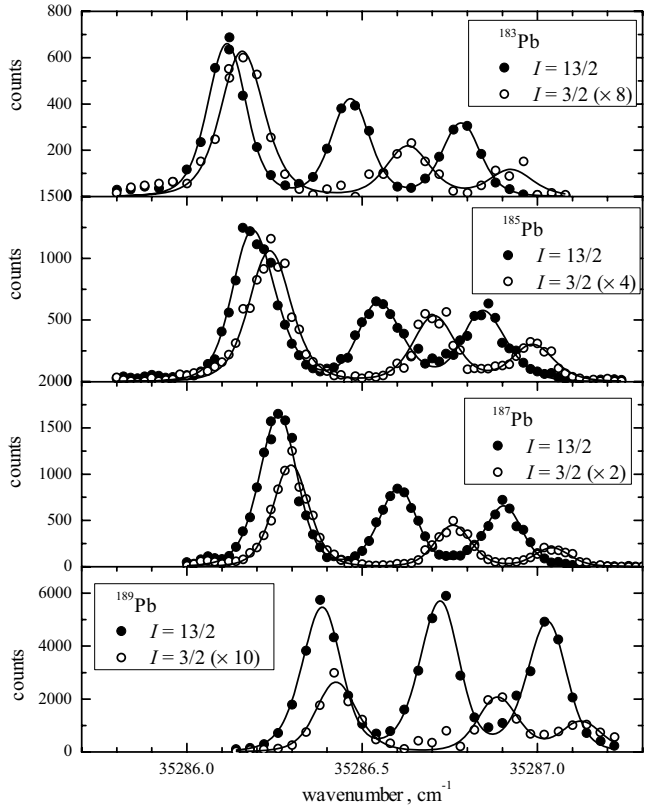

Fig. 2. Typical examples of the optical spectra collected in the individual scans. Here the dependence of the number of the detected photo-ions on the laser wave number $\tilde{\nu}$ ($\tilde{\nu} = 1/\lambda = c\nu$) is shown. Solid lines represent a fit to the data (see text).

Furthermore, for each isotope, measurements with a fixed reference laser frequency (close to the resonance) were performed after every three scanning steps as a means of monitoring the overall stability of the production, ionization, and detection system. In addition to the wavelength, the laser power in the first excitation step was recorded and used for correcting the measured intensities for power fluctuations. For an absolute wavelength scale calibration, spectra of stable Pb isotopes were also recorded regularly during the experimental period. For the stable isotopes, the photo-ion current was directly measured with a Faraday cup.

The properties of the radioactive Pb isotopes (spin, parity, half-life, α branching ratio), α- and/or γ-lines used for the detection, along with the parameters of the experimental set-up (implantation/measurement time and the estimated yield at the detection set-up) are presented in table 1.

3 Analysis

The atomic spectroscopic measurements have been performed using the $6p^2\ ^3P_0 \rightarrow 6p7s\ ^3P_1^o$ transition (the first excitation step, see fig. 1). For this transition the hyperfine splitting of the lower level ($J = 0$) is absent, therefore the position of the hyperfine components $\nu_0^{F'}$ in the optical spectrum is determined by the hyperfine splitting of the upper level ($J' = 1$) only:

$$\nu_0^{F'} = \nu_0 + A'\frac{K'}{2} + B'\frac{\frac{3}{4}K'(K'+1) - I(I+1)J'(J'+1)}{2(2I-1)(2J'-1)IJ'}, \quad (1)$$

where ν_0 is the position of the centre of gravity of the hyperfine splitting, $K' = F'(F'+1) - I(I+1) - J'(J+1)$, F is the total angular momentum of the atom ($\mathbf{F} = \mathbf{I}+\mathbf{J}$), A' and B' are the magnetic dipole and electric quadrupole hyperfine coupling constants, respectively, and the prime symbol denotes the excited atomic level.

After the corrections for laser power fluctuations and reference measurements the experimental optical spectra were fitted with a convolution of a Gaussian Doppler profile, corresponding to the ion source temperature, and a deformed Lorentzian profile representing the laser line shape. For more details see ref. [17]. The parameters ν_0, A' and B' were varied during the fit. The asymmetric laser line shape invoked an additional correction to obtain a value for ν_0, since the wavemeter readings corresponded not to the position of the maximum of the laser line, but to the position of its centre of gravity. To make this correction, for each spectrum the line shape deformation parameters, obtained from the fit of the same scan, were used.

The sign of the A' constant (and therefore the sign of the magnetic moment) can be deduced from the frequency ordering of the hfs components (see eq. (1)) in a similar way to other optical spectroscopic techniques. The hfs components corresponding to different F'-values were identified by their relative amplitudes $a_{F'}$. Our technique is based on the application of the 3-step photo-ionization, nevertheless the hfs relative amplitudes were dominated by the first-step hfs transition probabilities, which are proportional to $(2F'+1)$ for the selected transition. This is because the first-step transition was not or was only weakly saturated, while the second step was saturated by the broad-band laser with a linewidth larger than the hfs splitting and the third step in the photo-ionization scheme was non-resonant.

This method allowed us to reveal unambiguously the sign of magnetic coupling constant for low-spin states. For high-spin isomers, where the difference in transition probabilities for hfs components is much smaller than for low-spin states, an additional procedure was applied. To reduce the possible influence of the second step detuning and/or influence of the laser power fluctuations along the scan, the ratios of the amplitudes $(a^{ls}_{F'}/a^{hs}_{F'})$ of the most closely frequency-matching hfs components in the optical spectra of the high- and low-spin states (from the same scan) were also compared with the predicted values for the different signs of A.

3.1 Mean square charge radii

The isotopic change of the charge radius $\delta\langle r^2\rangle_{A,A'}$ was evaluated using the standard formula

$$\delta\nu_{A,A'} = F \cdot \lambda_{A,A'} + M\frac{A-A'}{A\cdot A'}\,, \tag{2}$$

where $\delta\nu_{A,A'}$ ($\delta\nu_{A,A'} = \nu_A - \nu_{A'}$) is the isotope shift between isotopes with mass numbers A and A', F is the electronic factor, M is the mass shift constant and $\lambda_{A,A'}$ is the nuclear parameter [30]:

$$\lambda = \delta\langle r^2\rangle + \frac{C_2}{C_1}\delta\langle r^4\rangle + \frac{C_3}{C_1}\delta\langle r^6\rangle + \ldots \approx C\delta\langle r^2\rangle. \tag{3}$$

The following values of constants were used [8]:

$F = 20.26\ (0.18)\,\mathrm{GHz}\cdot\mathrm{fm}^{-2}$,
$M = 0.19(25)\times N$ (where N is the normal mass shift constant [5]),
$C = 0.93$.

The effect of the nuclear shape on charge radii can be expressed as

$$\langle r^2\rangle_A \approx \langle r^2\rangle_A^{sph}\left(1 + \frac{5}{4\pi}\langle\beta_2^2\rangle_A\right), \tag{4}$$

where $\langle r^2\rangle_A^{sph}$ is the mean square radius of a spherical nucleus with the same volume. Usually for the evaluation of $\langle r^2\rangle_A^{sph}$ the droplet model is used [31].

3.2 Magnetic dipole moments and electric quadrupole moments

The magnetic dipole moments were evaluated from the scaling relations, based on the known magnetic moment μ_0, magnetic coupling constant A_0 and nuclear spin I_0 of the stable ^{207}Pb isotope ($\mu_0 = 0.592583(9)$ n.m., $I_0 = 1/2$, $A_0 = 8807.2(3.0)$ MHz [8,32]):

$$\mu = \frac{A\cdot I\cdot\mu_0}{A_0\cdot I_0}\,. \tag{5}$$

This expression disregards any hyperfine anomaly, which was found to be less than 10^{-3} for the $^{191-197}$Pb isotopes studied in ref. [7].

For the evaluation of the quadrupole moment, the semi-empirical expression from ref. [33] was used:

$$Q_S\ [e\cdot\mathrm{b}] = -0.00868(52)\times B\ [\mathrm{MHz}]\ (6p7s\ ^3P_1^{\mathrm{o}}). \tag{6}$$

For an axially deformed nucleus the intrinsic quadrupole moment Q_0 can be estimated using the following expression:

$$Q_S = \frac{3K^2 - I(I+1)}{(I+1)(2I+3)}Q_0, \tag{7}$$

where K is the projection of the nuclear spin on the symmetry axis of the nucleus. The intrinsic quadrupole moment Q_0, induced by the non-spherical charge distribution of the protons is then related to the nuclear charge deformation β_2 by

$$Q_0 \approx \frac{3}{\sqrt{5\pi}}eZR_0^2\left(\beta_2 + \frac{2}{7}\sqrt{\frac{5}{\pi}}\beta_2^2 + \ldots\right), \tag{8}$$

where the nuclear radius R_0 is usually calculated as $1.2\,A^{1/3}$ fm.

Table 2. Isotope shifts, hyperfine coupling constants, charge radii variations and electromagnetic moments for $^{182-190}$Pb.

Isotope	I^π	$\delta\nu_{A,208}$ (GHz)	A (GHz)	B (GHz)	$\delta\langle r^2\rangle_{A,208}$ (fm^2)^{a,b}	μ (n.m.)	Q_S (e·b)
^{182}Pb	0^+	−24.56(25)	–	–	−1.299(12){25}	–	–
^{183}Pb	$3/2^-$	−22.95(15)	−5.742(25)	−0.07(20)	−1.215(8){13}	−1.158(5)	0.6(18)
^{183m}Pb	$13/2^+$	−23.54(15)	−1.423(6)	−0.2(4)	−1.246(8){13}	−1.245(6)	1.7(35)
^{184}Pb	0^+	−21.74(10)	–	–	−1.150(5){13}	–	–
^{185}Pb	$3/2^-$	−20.66(15)	−5.652(25)	−0.03(15)	−1.093(8){13}	−1.141(5)	0.2(13)
^{185m}Pb	$13/2^+$	−21.26(15)	−1.405(12)	−0.11(15)	−1.125(8){13}	−1.23(1)	0.9(13)
^{186}Pb	0^+	−19.81(10)	–	–	−1.048(5){10}	–	–
^{187}Pb	$3/2^-$	−18.78(12)	−5.58(1)	0.05(20)	−0.993(6){10}	−1.126(3)	−0.4(17)
^{187m}Pb	$13/2^+$	−19.37(12)	−1.383(5)	0.06(30)	−1.025(6){10}	−1.210(5)	−0.5(25)
^{188}Pb	0^+	−17.57(12)	–	–	−0.930(6){10}	–	–
^{189}Pb	$3/2^-$	−16.82(15)	−5.36(4)	−0.06(20)	−0.890(8){10}	−1.081(9)	0.5(18)
^{189m}Pb	$13/2^+$	−17.36(20)	−1.36(1)	0.15(4)	−0.918(8){10}	−1.19(1)	−1.3(35)
^{190}Pb	0^+	−15.86(10)	–	–	−0.839(5){10}	–	–
^{190}Pb	0^+		–	–	−0.840{10}^{c}	–	–

^{a} Our data published in ref. [9].

^{b} The errors in round brackets reflect only the isotope shift uncertainties; the total errors (including the systematic errors which stem from the scaling uncertainty of the electronic factor and the specific mass shift) are given in the curly brackets.

^{c} Isotope shift measured for $6p^2\ ^1D_2 \longrightarrow 6p7s\ ^3P_1$ transition ($\lambda = 723$ nm) [7].

4 Results and discussion

Measured values of the isotope shifts, hfs coupling constants and the deduced values of the rms charge radii changes and nuclear moments are reported in table 2.

In the vicinity of mid-shell at $N = 104$ valence neutrons can occupy the $p_{3/2}$, $i_{13/2}$ and possibly $h_{9/2}$ sub-shells. The $h_{9/2}$ sub-shell for ^{183,185,187,189}Pb can be rejected because of a negative sign of the magnetic moment deduced for those isotopes. Furthermore, the spin and parity values of $I^\pi_{g.s.} = 3/2^-$ and $I^\pi_m = 13/2^+$ for the ground states and isomers were expected from the systematics, but other possible spin assignments were also investigated.

The occurrence of three hyperfine components in the optical spectra for the low-spin states excludes a $I = 1/2$ assignment (see eq. (1)) for those states. Moreover, fitting with the assumption $I = 5/2$ gives rise to a high value of the spectroscopic quadrupole moment $Q_S \geq 6.5(17)$ e·b for ^{183,185,187,189}Pb. Evaluating the intrinsic moment using eq. (7) with $K = I = 5/2$ gives $Q_0 \geq 18(5)$ e·b. This value corresponds to a strong quadrupole deformation of $\beta_2 \geq 0.52(15)$ (see eq. (8)), which is not consistent with the estimation of the deformation parameter ($\langle\beta_2^2\rangle^{1/2} < 0.2$ for $I = 5/2$) obtained from our $\delta\langle r^2\rangle$ measurements (see eq. (4)). This conclusion is not changed if it is assumed that $I = 5/2$ with $K = 1/2$ or $3/2$. So the expected spin assignment $I = 3/2$ for the low-spin states was confirmed.

For the high-spin states the situation is more complicated: due to large uncertainties of the obtained values of the coupling constant B' (and therefore Q_S), the comparison of the deformation parameters obtained from Q_S and $\delta\langle r^2\rangle$ measurements allows for the rejection of states with $I \leq 7/2$ only. Nevertheless, the negative sign of the magnetic moment seems to point to states originating from the $1\nu i_{13/2}$ sub-shell.

The charge radii variations for Pb isotopes and the droplet model predictions for various deformation values (see eq. (4)) are shown in fig. 3. The observed behaviour of the rms charge radii as a function of mass follows the smooth trend of the heavier isotopes down to, and even below, the neutron mid-shell at $N = 104$.

The deviation of the charge radii from the droplet model for the Pb isotopes with $N < 117$ is clearly seen in this figure. The full mean-field and IBM calculations [9] have shown that this deviation can be explained without the introduction of a static deformation, which is also in agreement with spectroscopic data [3,34] and with the quadrupole moments of ^{191,193}Pb [7].

In fig. 4 the isomeric changes of the charge radius ($\delta\langle r^2\rangle_{A^m,A} = \langle r^2\rangle_{A^m} - \langle r^2\rangle_{A^{g.s.}}$) for Pb and Hg isotopes with $N = 101$–116 are shown. Although no large isomeric shift was observed in the Pb isotopes, in the region of $N = 107$–115 the Pb and Hg isomers seem to behave in a similar way in that the sign of the isomeric shift changes from positive to negative with decreasing N. For the $^{183-189}$Pb isotopes the isomeric change of the charge radius remains practically constant (about -0.03 fm^2).

The similarity between Pb and Hg is also observed in the behaviour of the staggering parameter, which can be defined as

$$\gamma^*_{A+1} = 1 - \frac{2\delta\langle r^2\rangle_{A,A+1}}{\delta\langle r^2\rangle_{A,A+2}}, \quad \text{even } A. \tag{9}$$

This modified staggering parameter is related to γ, the staggering parameter introduced by Tomlinson and Stroke [35], as $\gamma^* = 1 - \gamma$, and is more illustrative since a higher value of γ^* corresponds to stronger staggering.

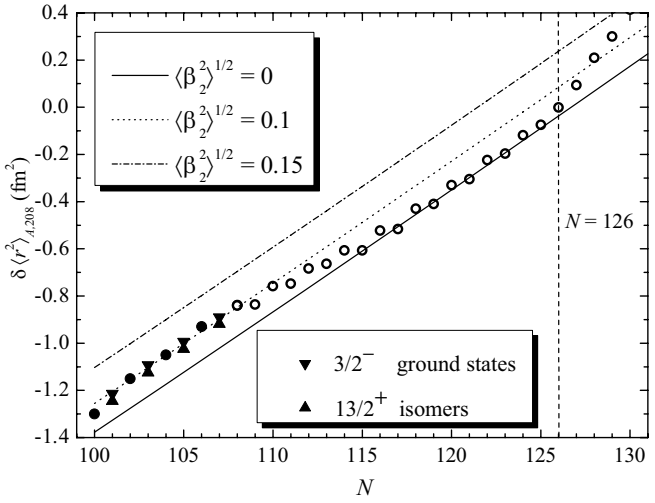

Fig. 3. Charge radii variations for the Pb isotopes compared with the droplet model predictions for various deformations, calibrated using $\langle\beta_2^2\rangle_{208}^{1/2} = 0.055$ [36]. Our data [9] are shown with filled symbols. Data from refs. [7,8] are shown with open circles. The error bars are smaller than the symbol size. Note: in fig. 2 in ref. [9] the marking for ground and isomeric states for odd-A isotopes is made incorrectly.

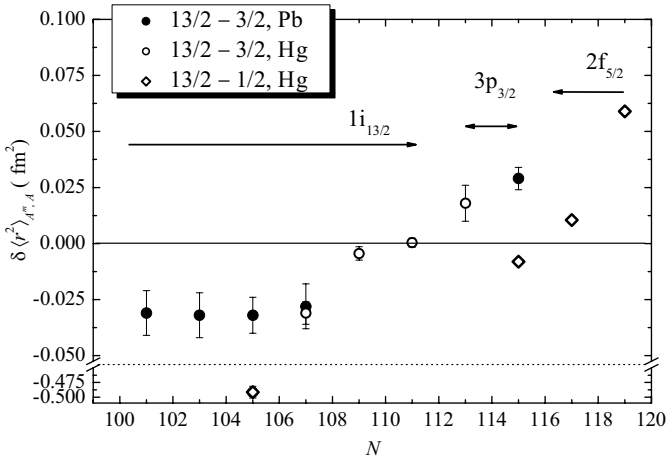

Fig. 4. Charge radii difference between $13/2^+$ isomeric states and $3/2^-$ (circles) or $1/2^-$ (diamonds) ground states for Pb and Hg [9,7,8,37]. On top of the figure the relevant neutron orbitals are given.

The staggering parameter for Pb and Hg as a function of the neutron number is shown in fig. 5. The trend for the $3/2^-$ states of Pb and Hg is similar, as well as the trend for isomers with $I = 13/2^+$ and $N > 109$. In contrast to the Hg isotopic chain no strong staggering has been observed in the Pb isotopes with $102 \leq N \leq 106$. For Hg $13/2^+$ isomers the staggering parameter is increasing monotonically as a function of the lowering neutron number, but for the $13/2^+$ Pb isomers the staggering reaches its maximum at $N = 107$–109.

Figure 6 presents the magnetic moments, obtained for the 3/2 and 13/2 states in this work, along with

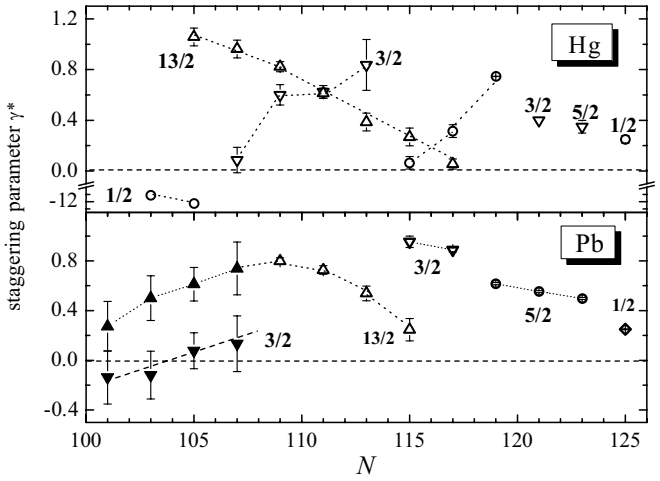

Fig. 5. Isotopic variation of the staggering parameter γ_A^*. For Pb isotopes $\gamma_{183-189}^*$ is calculated using our data from ref. [9] and $\gamma_{191-202}^*$ is taken from refs. [7,8]. For Hg isotopes γ^* is taken from ref. [37]. Lines connecting data points are shown only to guide the eye. Our data for Pb isotopes are shown with filled symbols.

the values for the 13/2 isomers of the heavier Pb isotopes [7]. The experimental data are close to the single-particle values for ^{207}Pb ($\mu(1i_{13/2}) = -1.144$ n.m. and $\mu(3p_{3/2}) = -1.227$ n.m.), calculated by Bauer *et al.* [38] using effective g-factors, taking into account configuration mixing, core polarization and mesonic effects.

First of all, we stress the similar linear trend of the magnetic moments for the $13/2^+$ isomers in the heavier

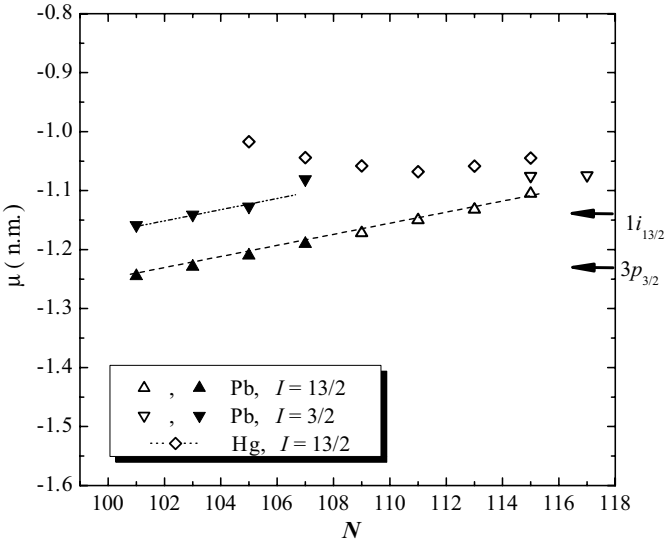

Fig. 6. Magnetic moments for the neutron-deficient odd-A lead isotopes. Our data are shown with filled triangles, data from ref. [7] with the open triangles, magnetic moments for Hg are taken from refs. [39,40]. The line connecting the data point for high-spin isomers is to guide the eye only. The arrows indicate the single-particle values for ^{207}Pb [38]. The error bars are smaller than the symbol size.

Hg and Pb isotopes with $111 \leq N \leq 115$. This reflects the well-established fact that both underlying even-even Hg and Pb cores are spherical in the heavier nuclei and the coupling of an odd neutron does not change the configuration or deformation [3]. In particular, the magnetic moments of the 13/2 isomers in $^{191-197}$Pb isotopes follow a linear trend with a slight down-sloping evolution towards the Schmidt line ($\mu_{Schm} = -1.91$ n.m.). The fact that the magnetic moments for the $13/2^+$ states in the lighter odd-A $^{183-189}$Pb isotopes, measured in this work, continue the same trend confirms their similarity to the spherical heavier Pb isotopes. In the same way, the linear trend of the magnetic moments of the $3/2^-$ isomers for the odd-A $^{183-189}$Pb isotopes and their closeness to the single-particle calculations for almost spherical ^{207}Pb [38] also confirms the predominantly spherical single-particle character of the 3/2 states in the lightest Pb isotopes.

In contrast to this, the trend for the $13/2^+$ isomers for the light isotopes ($N < 111$) is different for Hg and Pb nuclei. This might reflect the difference between the underlying cores in the respective even-even Pb and Hg chains as the neutron mid-shell is approached. Indeed, while the Pb nuclei in the vicinity of $N = 104$ stay predominantly spherical, as shown by in-beam, decay and charge radii work [1–4,9], a transition from a nearly spherical shape in heavier Hg isotopes (up to $N = 110$) to a weakly oblate deformed core happens in the Hg isotopes, as confirmed by numerous studies, see *e.g.* ref. [3] and references therein.

5 Conclusions

The in-source laser resonance ionization spectroscopy technique has become a very efficient tool for investigations of rare isotopes approaching the driplines. Experiments performed at the ISOLDE facility have shown that the extreme sensitivity of in-source laser spectroscopy combined with synchronous nuclear decay spectroscopy allows us to explore the heavy-mass regions very far from stability down to isotopes produced at a rate of a few ions per second. Our data show that, as has been reported for the even-even Pb isotopes, the neutron-deficient odd-A Pb nuclei are essentially spherical, up to and beyond the neutron mid-shell at $N = 104$.

This work was supported in part by FWO-Vlaanderen (Belgium), GOA/2004/03 (BOF-K.U. Leuven), Interuniversity Attraction Poles Programme - Belgian State - Belgian Science Policy (BriX network P6/23), German Ministry for Education and Research (BMBF, contract no. 06 MZ 171) and the European Commission within the Sixth Framework Programme through I3-EURONS (Contract RII3-CT-2004-506065). We would like to thank the ISOLDE collaborators for their technical assistance and cooperation.

References

1. A.N. Andreyev *et al.*, Nature **405**, 430 (2000).
2. K. Van de Vel *et al.*, Phys. Rev. C **65**, 064301 (2002).
3. R. Julin *et al.*, J. Phys. G **27**, R109 (2001).
4. J. Pakarinen *et al.*, Phys. Rev. C **75**, 014302 (2007).
5. E.W. Otten, in *Treatise on Heavy-Ion Science*, edited by D.A. Bromley, Vol. **8** (Plenum Press, New York, 1989) p. 517.
6. H.-J. Kluge, W. Nörtershäuser, Spectrochim. Acta B **58**, 1031 (2003).
7. S.B. Dutta *et al.*, Z. Phys. A **341**, 39 (1991).
8. M. Anselment *et al.*, Nucl. Phys. A **451**, 471 (1986).
9. H. de Witte *et al.*, Phys. Rev. Lett. **98**, 112502 (2007).
10. J. Bonn *et al.*, Phys. Lett. B **38**, 308 (1972).
11. G.D. Alkhazov *et al.*, Nucl. Instrum. Methods B **69**, 517 (1992).
12. A.E. Barzakh *et al.*, Phys. Rev. C **61**, 034304 (2000).
13. V.N. Fedosseev *et al.*, Nucl. Instrum. Methods B **204**, 353 (2003).
14. A.N. Andreyev *et al.*, Eur. Phys. J. A **14**, 63 (2002).
15. U. Köster *et al.*, Nucl. Instrum. Methods B **204**, 347 (2003).
16. J. Sauvage *et al.*, Eur. Phys. J. A **39**, 33 (2009).
17. H. De Witte, PhD Thesis, K.U. Leuven, Leuven, 2004.
18. B.A. Marsh, PhD Thesis, University of Manchester, Manchester, 2007.
19. K.S. Toth *et al.*, Phys. Rev. C **60**, 011302 (1999).
20. D.G. Jenkins *et al.*, Phys. Rev. C **62**, 021302 (2000).
21. D.G. Jenkins *et al.*, Phys. Rev. C **66**, 011301 (2002).
22. K. Van de Vel *et al.*, Phys. Rev. C **68**, 054311 (2003).
23. J.F.C. Cocks *et al.*, Eur. Phys. J. A **3**, 17 (1998).
24. R.B. Firestone, *Table of Isotopes* (Wiley, New York, 1996) p. 2372.
25. A.N. Andreyev *et al.*, J. Phys. G **25**, 835 (1999).
26. A.N. Andreyev *et al.*, Phys. Rev. C **66**, 014313 (2002).
27. U.J. Schrewe *et al.*, Phys. Lett. B **91**, 46 (1980).
28. J. Wauters *et al.*, Z. Phys. A **345**, 21 (1993).
29. J. Wauters *et al.*, Z. Phys. A **342**, 277 (1992).
30. E.C. Seltzer, Phys. Rev. **188**, 1916 (1969).
31. W.D. Myers, K.H. Schmidt, Nucl. Phys. A **410**, 61 (1983).
32. O. Lutz, G. Stricker, Phys. Lett. A **35**, 397 (1971).
33. J. Dembczynski, H. Rebel, Z. Phys. A **315**, 137 (1984).
34. T. Grahn *et al.*, Phys. Rev. Lett. **97**, 062501 (2006).
35. W.J. Tomlinson, H.H. Stroke, Nucl. Phys. **60**, 614 (1964).
36. S. Raman *et al.*, At. Data Nucl. Data Tables **78**, 1 (2001).
37. G. Ulm *et al.*, Z. Phys. A **325**, 247 (1986).
38. R. Bauer *et al.*, Nucl. Phys. A **209**, 535 (1973).
39. P. Dabkiewicz *et al.*, Phys. Lett. B **82**, 199 (1979).
40. R.J. Reimann, M.N. McDermott, Phys. Rev C **7**, 2065 (1973).